Nontrivial effect of out-of-plane acoustic phonon mode on limiting room temperature conductivity of ABA-stacked trilayer graphene

Lanting Feng,[1] Zhe Liu,[2] Mingfeng Zhu,[1,*] and Yisong Zheng[1,†]

[1]*Key Laboratory of Physics and Technology for Advanced Batteries (Ministry of Education) and Department of Physics, Jilin University, Changchun 130012, China*

[2]*Institute for Advanced Study, Shenzhen University, Shenzhen 518060, China*

(Received 4 January 2022; revised 24 April 2022; accepted 20 May 2022; published 26 May 2022)

The ABA-stacked trilayer graphene (TLG) has a parabolic dispersion band spanning the Fermi level, apart from the linear dispersion band which is almost a duplicate of that in monolayer graphene (MLG). Such a band structure implies that the TLG is a metal and seemingly has a larger conductivity than MLG due to the additional contributions of the parabolic bands when the linear dispersion bands in TLG and MLG host the same number of carriers. However, our numerical calculations indicate that the conductivity of TLG is smaller than that in MLG roughly by 20% when a moderate carrier doping drives the Fermi energy away from the Dirac point by at least 50 meV. To explain such a disagreement between the band structure and the conductivity, we find that the out-of-plane atomic vibration, i.e., the so-called *ZA* phonon mode in the long-wavelength region, plays a critical role in limiting the conductivity of TLG due to the strong interband scattering. In contrast to MLG, such a *ZA* phonon mode is completely decoupled from the electron-phonon scattering due to the symmetry incompatibility.

DOI: 10.1103/PhysRevB.105.195433

I. INTRODUCTION

Graphene multilayers, i.e., the combined graphene monolayers by van der Waals interlayer interactions, have attracted considerable attention due to their abundant electronic properties that depend on the stacking order [1–18]. For instance, there exist two kinds of allotrope of trilayer graphene (TLG) in terms of stacking order. As shown in Fig. 1, the first one of the TLG obeys the Bernal or ABA stacking, where the atoms of the topmost layer lie exactly on the top of the bottom layer. And the other is called the rhombohedral or ABC-stacked TLG, where one sublattice of the top layer lies above the center of the hexagons in the bottom layer. So far, large-scale synthesis of high-quality TLGs in the two stacking orders has both been realized experimentally [19,20], which provides an extra platform for designing graphene-based electronic devices. The low-energy band structure around the Fermi energy of ABA-stacked TLG consists of a combination of the linear dispersion of monolayer graphene (MLG) and the quadratic dispersion of bilayer graphene, whereas the electronic dispersion of ABC-stacked TLG is approximately cubic, with its conduction and valence bands touching at a point close to the highly symmetric K and K' points in the Brillouin zone (BZ). The distinctive band structures of the two kinds of TLG are expected to give rise to different transport properties [2,5,21].

It is well known that electron-phonon interaction is ubiquitous in solids which is associated with many electronic properties of materials, such as the conventional superconductivity, the intrinsic resistivity of metals and carrier mobility of semiconductors. Some works have studied the conventional phonon-mediated superconducting properties of TLG experimentally and theoretically [13,16,17,22]. Recently, two works by Zhou *et al.* reported the experimental observation of superconductivity and ferromagnetism in ABC-stacked TLG even without an interlayer magic-angle twist [13,17], which poses a new perspective to the origin of superconductivity in the graphene based systems. A sequent theoretical study provided a simple explanation for the two distinct superconducting phases of TLG observed in the experiment by assuming the electron-acoustic-phonon coupling as the possible electronic pairing mechanism [16]. Apart from the phonon-mediated superconductivity, electron-phonon interaction also play an important role on limiting the electronic transport in metallic and semiconducting materials such as the TLGs. In particular, at room temperature, the electron-phonon interaction becomes the dominating scattering mechanism for limiting the electronic transport property. Like the MLG, the TLGs are also two-dimensional planar materials. Therefore carrier polarity (electron/hole) and concentration can be realized and adjusted by gating effect besides the conventional chemical doping. For the device applications of TLGs, it is absolutely necessary to have a complete understanding about the electronic transport properties of TLGs at room temperature, especially, in comparison with the case of MLG. As aforementioned, the ABA-stacked TLG has a pair of the linear dispersion bands which bears a high analogy with their counterpart in graphene monolayer. However, besides the linear band, it has an extra parabolic band spanning the Fermi level. Hence, in contrast to the case of MLG, the ABA-stacked TLG has more electronic states in a certain energy shell around the Fermi level to take part in the electronic transport under a driving electric field. This implies that the intrinsic conductivity of ABA-stacked

*Corresponding author: mfzhu@jlu.edu.cn
†Corresponding author: zhengys@jlu.edu.cn

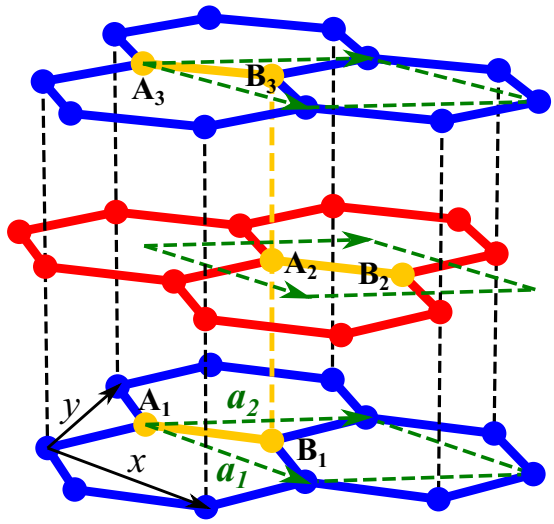

FIG. 1. Structure of ABA-stacked TLG. The atoms inside one unit cell are plotted in orange and labeled by A_1, B_1, A_2, B_2, A_3, and B_3 with A_i and B_i in ith layer. $\boldsymbol{a}_1$ and $\boldsymbol{a}_2$ are the in-plane lattice vectors.

TLG should be larger than that in MLG from the viewpoint of the electronic band structure. In fact, apart from its effect of the electronic structure, the interlayer coupling distinguishes the ABA-stacked TLG from MLG also in the phonon dispersion and the electron-phonon interaction. Therefore it becomes much complicated to predict the electronic transport property subject to the electron-phonon scattering. To sum up the above statements from the conventional superconductivity and the electron-phonon scattering limited electronic transport, there is a need to perform a systematic study on the e-ph interaction in TLGs on the level of first-principles calculations beyond the simple theoretical models. Such a theoretical study is desirable for quantitatively explaining the relevant experimental observation. However, to the best of our knowledge, any first-principles study on the e-ph interaction and the associated physical properties such as the intrinsic conductivity of TLGs is yet lacking.

In this paper, the e-ph scattering limited conductivity of ABA-stacked TLG at room temperature is calculated by using the iterative Boltzmann transport equation (BTE). And all transport properties of ABA-stacked TLG are compared with those of MLG. All the required quantities are obtained via the first-principles calculations and free from any empirical parameters. Our numerical calculations indicate that the conductivity of ABA-stacked TLG is smaller than that in MLG, though the former has one more band spanning the Fermi level than the latter. By a detailed analysis, we find that the out-of-plane vibration, i.e., the ZA phonon mode in the long-wavelength region, plays the critical role on limiting the conductivity of ABA-stacked TLG. Moreover, in view of the ultrahigh conductivity of MLG, our numerical result indicates that the ABA-stacked TLG is still a good conductor under a moderate carrier doping. For simplicity, the TLG we mention hereinafter only means ABA-stacked TLG unless it is stated explicitly because we focus on only the intrinsic conductivities of ABA-stacked TLG in this paper.

The rest of the present work is organized as follows. In Sec. II, we give a brief description of the theoretical methods, including the technology details of the first-principles calculations and the formulas for calculating the intrinsic conductivity. In Sec. III, numerical results are presented and discussed. Finally, we summarize the main conclusions in Sec. IV.

II. COMPUTATIONAL METHOD

To investigate the e-ph scattering limited conductivity of TLG on the level of first-principles calculations, the electronic and phononic dispersions and the e-ph coupling matrix elements of TLG and MLG are calculated within the DFT [23] and DFPT [24] frameworks firstly. Then, the e-ph scattering limited conductivity driven by an electric field in a given direction is calculated according to the linearized BTE [25,26], which reads

$$\sigma = \frac{2e^2}{N_k \Omega k_B T} \sum_{n\boldsymbol{k}} f_{n\boldsymbol{k}}(1 - f_{n\boldsymbol{k}})(\boldsymbol{v}_{n\boldsymbol{k}} \cdot \boldsymbol{\epsilon})(\boldsymbol{F}_{n\boldsymbol{k}} \cdot \boldsymbol{\epsilon}), \tag{1}$$

where e, k_B, and T are the elementary charge, Boltzmann constant, and temperature, respectively, $f_{n\boldsymbol{k}}$ is the Fermi-Dirac distribution for the electronic state $\varphi_{n\boldsymbol{k}}$ with n and $\boldsymbol{k}$ being the band index and wave vector, $\boldsymbol{\epsilon}$ is the unit vector in the electric field direction, N_k is the number of the $\boldsymbol{k}$ points for sampling the BZ, Ω stands for the unit cell area, and $\boldsymbol{v}_{n\boldsymbol{k}}$ is the electron velocity, defined by $\boldsymbol{v}_{n\boldsymbol{k}} = \nabla E_{n\boldsymbol{k}}/\hbar$. For two-dimensional materials, the conductivity and the conductance have the same unit of Siemens (S), the inverse of ohm.

In Eq. (1), $\boldsymbol{F}_{n\boldsymbol{k}}$ is referred to as the electron free path associated with the e-ph scattering which satisfies the linearized BTE

$$\boldsymbol{F}_{n\boldsymbol{k}} = \boldsymbol{v}_{n\boldsymbol{k}}\tau_{n\boldsymbol{k}} + \tau_{n\boldsymbol{k}} \sum_{m\boldsymbol{q}\nu} \left(G^{m\boldsymbol{k}+\boldsymbol{q}}_{n\boldsymbol{k},-\boldsymbol{q}\nu} + G^{m\boldsymbol{k}+\boldsymbol{q}}_{n\boldsymbol{k},\boldsymbol{q}\nu}\right)\boldsymbol{F}_{m\boldsymbol{k}+\boldsymbol{q}} \tag{2}$$

with

$$G^{m\boldsymbol{k}+\boldsymbol{q}}_{n\boldsymbol{k},-\boldsymbol{q}\nu} = \frac{2\pi}{\hbar}\left|g^{m\boldsymbol{k}+\boldsymbol{q}}_{n\boldsymbol{k},\boldsymbol{q}\nu}\right|^2 (1 + N_{-\boldsymbol{q}\nu} - f_{m\boldsymbol{k}+\boldsymbol{q}}) \times \delta(E_{n\boldsymbol{k}} - \hbar\omega_{-\boldsymbol{q}\nu} - E_{m\boldsymbol{k}+\boldsymbol{q}}) \tag{3}$$

and

$$G^{m\boldsymbol{k}+\boldsymbol{q}}_{n\boldsymbol{k},\boldsymbol{q}\nu} = \frac{2\pi}{\hbar}\left|g^{m\boldsymbol{k}+\boldsymbol{q}}_{n\boldsymbol{k},\boldsymbol{q}\nu}\right|^2 (N_{\boldsymbol{q}\nu} + f_{m\boldsymbol{k}+\boldsymbol{q}}) \times \delta(E_{n\boldsymbol{k}} + \hbar\omega_{\boldsymbol{q}\nu} - E_{m\boldsymbol{k}+\boldsymbol{q}}), \tag{4}$$

where $\boldsymbol{q}$, $E_{n\boldsymbol{k}}$, $\omega_{\boldsymbol{q}\nu}$ and $N_{\boldsymbol{q}\nu}$ denote the phonon wave vector, electronic energy, phonon frequency, and the phonon Boson distribution function, respectively. $g^{m\boldsymbol{k}+\boldsymbol{q}}_{n\boldsymbol{k},\boldsymbol{q}\nu}$ is the scattering matrix element, which stands for the electron transition from state $\varphi_{n\boldsymbol{k}}$ to state $\varphi_{m\boldsymbol{k}+\boldsymbol{q}}$ with a phonon in state $\phi_{\nu\boldsymbol{q}}$ emitted or absorbed. It takes the form

$$g^{m\boldsymbol{k}+\boldsymbol{q}}_{n\boldsymbol{k},\boldsymbol{q}\nu} = \langle\varphi_{m\boldsymbol{k}+\boldsymbol{q}}|\partial_{\boldsymbol{q}\nu}V|\varphi_{n\boldsymbol{k}}\rangle. \tag{5}$$

The derivative of the potential is defined as

$$\partial_{\boldsymbol{q}\nu}V = \sqrt{\frac{\hbar}{2M\omega_{\boldsymbol{q}\nu}}} \sum_{\boldsymbol{R}s\alpha} \partial_{\boldsymbol{R}s\alpha}V(\boldsymbol{r}, \boldsymbol{R}s\alpha)\boldsymbol{e}^{\boldsymbol{q}\nu}_{\boldsymbol{R}s\alpha} e^{i\boldsymbol{q}\cdot\boldsymbol{R}}, \tag{6}$$

where M is the atom mass of carbon, s denotes an atom inside the unit cell positioned by the lattice vector $\boldsymbol{R}$, which can be A_1, B_1, A_2, B_2, A_3, and B_3 as shown in Fig. 1, α (=x, y or z) stands for the vibration direction of atom s, $\boldsymbol{e}^{\boldsymbol{q}\nu}_{\boldsymbol{R}s\alpha}$ is the $\boldsymbol{R}s\alpha$ component of phonon eigenvector $\boldsymbol{e}^{\boldsymbol{q}\nu}$, and $\partial_{\boldsymbol{R}s\alpha}V$ is the derivative of potential with respect to the atomic displacement.

In Eq. (2), $\tau_{n\boldsymbol{k}}$ stands for the relaxation time, the inverse of which represents the scattering rate due to e-ph coupling which reads

$$\frac{1}{\tau_{n\boldsymbol{k}}} = \frac{2\pi}{\hbar}\sum_{m\boldsymbol{q}\nu}\left|g^{m\boldsymbol{k}+\boldsymbol{q}}_{n\boldsymbol{k},\boldsymbol{q}\nu}\right|^2[(1+N_{-\boldsymbol{q}\nu}-f_{m\boldsymbol{k}+\boldsymbol{q}})\delta(E_{n\boldsymbol{k}}-\hbar\omega_{-\boldsymbol{q}\nu}-E_{m\boldsymbol{k}+\boldsymbol{q}})+(N_{\boldsymbol{q}\nu}+f_{m\boldsymbol{k}+\boldsymbol{q}})\delta(E_{n\boldsymbol{k}}+\hbar\omega_{\boldsymbol{q}\nu}-E_{m\boldsymbol{k}+\boldsymbol{q}})]. \tag{7}$$

To solve Eq. (2) numerically, the iteration approach is adopted to obtain the electron free path. During the iteration, the values of $\boldsymbol{F}'_{m\boldsymbol{k}+\boldsymbol{q}}$s were guessed for the first iteration step, then they were put into the right-hand side of Eq. (2) to update the values of $\boldsymbol{F}'_{n\boldsymbol{k}}$s as the second guess. Such an iteration procedure is repeated until convergence.

If the second term to the right-hand side of Eq. (2) is neglected, we have the approximate solution of the electronic free path as $\boldsymbol{F}_{n\boldsymbol{k}} = \boldsymbol{v}_{n\boldsymbol{k}}\tau_{n\boldsymbol{k}}$. Consequently, Eq. (1) is simplified into

$$\sigma = \frac{2e^2}{N_k\Omega k_B T}\sum_{n\boldsymbol{k}} f_{n\boldsymbol{k}}(1-f_{n\boldsymbol{k}})(\boldsymbol{v}_{n\boldsymbol{k}}\cdot\boldsymbol{\epsilon})^2\tau_{n\boldsymbol{k}}. \tag{8}$$

Such a treatment is called energy relaxation time approximation (ERTA), which was widely employed to deal with the e-ph scattering limited conductivity [27,28]. However, the accuracy of ERTA should be checked by comparing with the iteration solution of the BTE if one want to explain or predict the conductivity of a material accurately.

In order to calculate the conductivity of TLG and MLG according to Eqs. (1)–(7), the electronic eigenenergy $E_{n\boldsymbol{k}}$, phonon frequency $\omega_{\boldsymbol{q}\nu}$ and e-ph scattering matrix element $g^{m\boldsymbol{k}+\boldsymbol{q}}_{n\boldsymbol{k},\boldsymbol{q}\nu}$ on an ultradense $\boldsymbol{k}$ and $\boldsymbol{q}$ mesh are needed. Two steps of the calculations are adopted in this paper. Firstly, we take relatively coarse 16×16 $\boldsymbol{k}$ mesh and 8×8 $\boldsymbol{q}$ mesh to calculate the electron band structures, phonon dispersion and e-ph scattering matrix by using DFT and DFPT methods implemented in QUANTUM ESPRESSO package [29]. For these calculations, the norm-conserving pseudopotential [30], the exchange-correlation functional with the generalized gradient approximation proposed by Perdew-Burke-Ernzerhof [31], and the kinetic energy cutoff of 150 Ry are adopted. The van der Waals interaction was included by considering the DFT-D correction. A large vacuum space of 20 Å along the z direction was used to avoid the interactions between the periodic images. Then the Wannier interpolation technique [32] realized by EPW code [33] is adopted to obtain the values of $E_{n\boldsymbol{k}}$, $\omega_{\boldsymbol{q}\nu}$, and $g^{m\boldsymbol{k}+\boldsymbol{q}}_{n\boldsymbol{k},\boldsymbol{q}\nu}$ on an ultradense 600×600 $\boldsymbol{k}$ mesh and 600×600 $\boldsymbol{q}$ mesh.

III. NUMERICAL RESULTS AND DISCUSSIONS

A. Electronic structures and phonon band dispersions

The crystal structure of TLG is shown in Fig. 1. The optimized interlayer spacing and in-plane lattice constant are 3.24 and 2.46 Å, respectively. The band structure and its zoom-in around K point and in the vicinity of the Fermi energy are shown in Figs. 2(a) and 2(b). The band structure around K' point is the same as those around K due to the symmetry and not shown. The results indicate that there are a pair of linear dispersion bands and a pair of parabolic dispersion bands near the Fermi energy, which is almost a combination of a MLG and a bilayer graphene except for the small but observable gaps. The appearance of the small gaps is mainly attributed to the nonzero interlayer hopping energy [34]. As shown in Fig. 2(b), the four bands of TLG around the Fermi energy are labeled by 1, 2, 3, and 4. Bands 1 and 4 (2 and 3) are linear (parabolic) bands and bands 1 and 2 (3 and 4) are at the hole (electron) side. Besides, the linear dispersion bands in TLG have a slightly upward shift (0.013 eV) relative to MLG. But they have almost the same Fermi velocity. In order to present our results conveniently, we define the Dirac point of TLG as the extrapolated intersection of the linear bands inside the small band gap [see Fig. 2(c)]. So the Dirac point of TLG is located at 0.013 eV above the charge neutrality point.

The comparison of the phonon dispersions between TLG and MLG are shown in Figs. 3(a) and 3(b). The results indicate that the phonon modes of TLG are the same as those of MLG and triply degenerate over almost the whole BZ except for the region around Γ point. In terms of the long-wavelength vibration characteristics, the phonons in TLG can be classified as out-of-plane acoustic (ZA), transverse acoustic (TA), longitudinal acoustic (LA), out-of-plane optical (ZO), transverse optical (TO), and longitudinal optical (LO) vibration modes. Around Γ point, the triple degeneracies of the acoustic branches are obviously lifted. The ZA mode in MLG splits into one ZA and two ZO modes in TLG [see Fig. 3(b)]. For the evolution of ZA mode from MLG to TLG, the three layers can vibrate synchronously and asynchronously in TLG, although the two nonequivalent carbon atoms inside one layer vibrate synchronously along the z direction. That three layers vibrate synchronously corresponds to the lowest frequency of the three split phonon branches with vanishing frequency in the long-wavelength limit, that is the ZA mode in TLG. For the other two branches, the three layers vibrate asynchronously, namely two optical branches with higher frequency in TLG. Therefore, after introducing another two layers, the acoustic ZA mode in MLG evolve into one acoustic plus two optical modes in TLG. The other two acoustic modes TA and LA undergo the similar degeneracy lifting. Please refer to Ref. [35] for more details about the phonon dispersions in TLG.

B. Electron-phonon coupling and intrinsic conductivity

In contrast to the conductivity due to impurity or defect scattering, we refer to the conductivity due to phonon

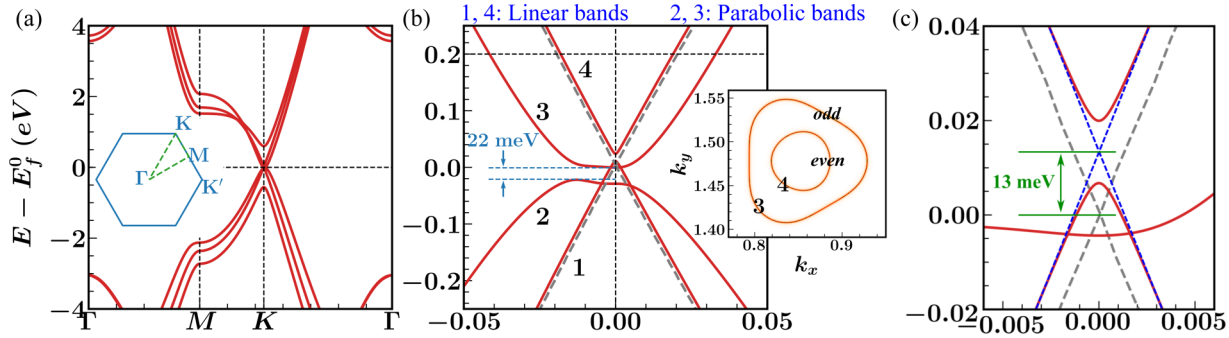

FIG. 2. (a) Band structure of TLG with inset showing the BZ and special k points. (b) Four bands of TLG (red solid lines labeled by 1, 2, 3, and 4) and two bands of MLG (gray dashed lines) around K point. The charge neutrality point E_f^0 is used as the energy reference in both two subplots. The linear bands in TLG (bands 1 and 4) have a shift of 0.013 eV upwards relative to those of MLG. Inset in (b) is the Fermi surface for energy at 0.2 eV. The eigenstates in bands 3 and 4 have the odd and even parity with respect to the mirror reflection $\hat{M}_z$. (c) The zoom-in of the band structures around the Dirac points of TLG and MLG. The linear bands of TLG are fitted by dashed blue lines and the intersection is defined as the Dirac point of TLG, which is above the Dirac point of MLG by 0.013 eV.

scattering as the intrinsic conductivity, because e-ph scattering is inevitable even in a perfect lattice. We restrict our interest on the intrinsic conductivity of TLG at 300 K because the e-ph interaction is the leading scattering mechanism in metals and semiconductors at room temperature in spite of the presence of other kinds of scatterings, such as defects, interfaces, impurities, and so on. In order to make a quantitative comparison of the calculated conductivity between the TLG and MLG, we align their Dirac points as the energy reference. Thus, at a specific Fermi energy, the linear band of the TLG has the Fermi surface with the same size as that in MLG.

First of all, we compare the conductivities of TLG by using the iteration method and ERTA as shown in Fig. 4(a). The results indicate the ERTA predicts smaller conductivities than

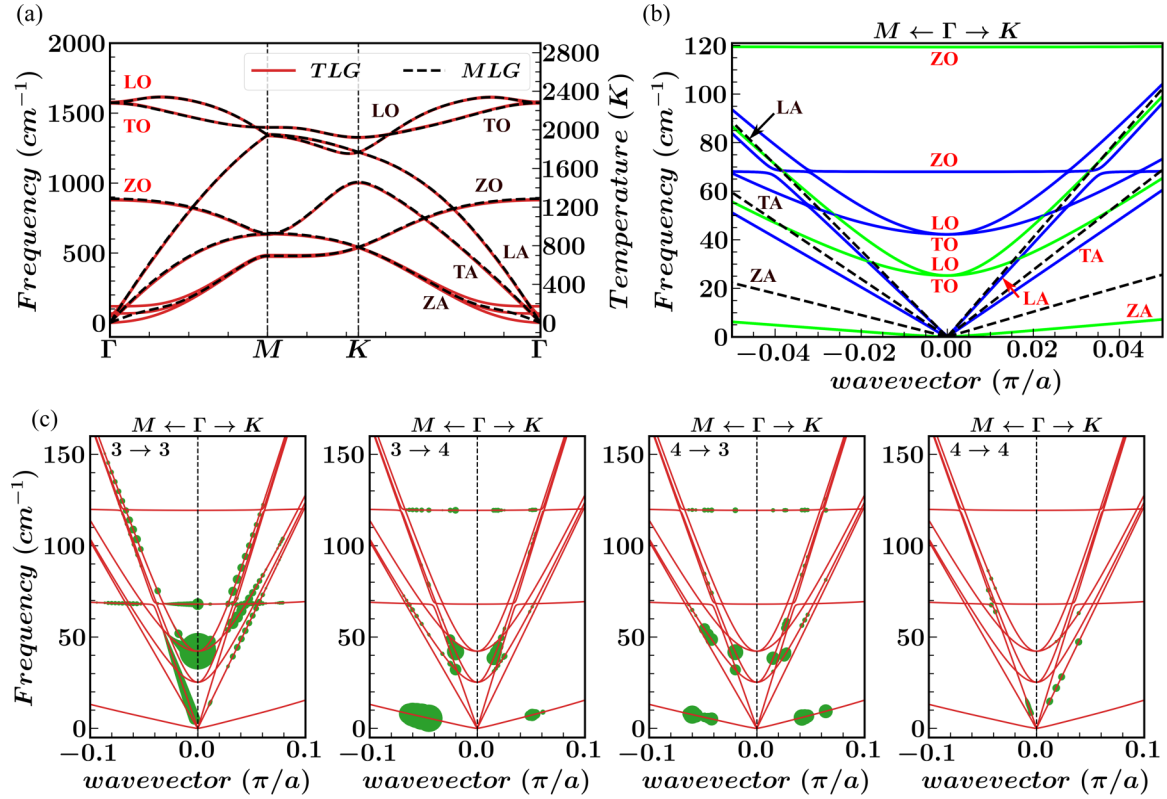

FIG. 3. (a) Phonon dispersions of TLG (red solid lines) and the comparison with that of MLG (black dashed lines). (b) Zoom-in of phonon dispersions around Γ point. The blue and green solid lines stand for the phonon modes of TLG with odd and even parity, respectively, with respect to the mirror reflection M_z. Note that the even-parity phonons do not take part in the intraband e-ph scattering. The phonon modes of MLG are plotted in black dashed lines for comparison. (c) Phonon mode resolved e-ph scattering strength $\gamma_{nm}^{\nu}(\boldsymbol{q})$ for the intraband ($3 \to 3$ and $4 \to 4$) and interband ($3 \to 4$ and $4 \to 3$) scatterings at $E_f = 0.2$ eV. Stronger scattering strength is denoted by the green dot with larger size. Bands 3 and 4 are the parabolic and linear bands, respectively, as shown in Fig. 2.

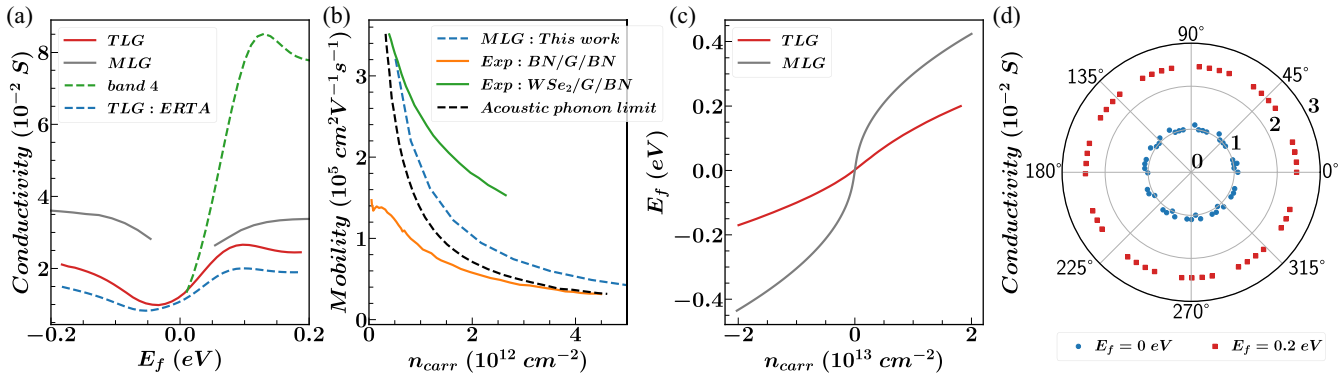

FIG. 4. (a) Intrinsic conductivities of TLG and MLG calculated by the iteration method with the Dirac points of MLG and TLG used as the energy references to make sure the linear bands in MLG and TLG show the same Fermi surface. The conductivities of TLG calculated under the ERTA are also shown in blue dashed line for comparison. The green dashed line gives the conductivity of TLG with only the contribution of band 4 (the linear band as shown in Fig. 2) and the intraband scattering. (b) The comparison of mobilities of MLG with previous theoretical and experimental results. Our results for MLG are plotted in blue dashed lines. The experimental data are from graphene (G) heterostructures of BN/G/BN [36] and WSe_2/G/BN [37]. The black dashed line is the mobility limit due to the acoustic phonon scattering with uncertainties of the order of 20% at most, and the data is extracted directly from Ref. [37]. (c) The relationship between Fermi energy and carrier concentration for TLG and MLG. (d) Intrinsic conductivity of TLG along various directions. In (c) and (d), the Fermi energy E_f is measured relative to the charge neutrality point.

the iteration method especially at the relatively large Fermi energy, so it is necessary to perform the iteration procedure to obtain the quantitatively accurate conductivity of TLG, although the two methods predict the similar trend in conductivity with the change of Fermi energy. Therefore we discuss only the results obtained by the iteration method hereafter. In Fig. 4(b), we compare our calculated mobility of MLG with previous theoretical and experimental results [36,37]. The acoustic phonon limit curve in Fig. 4(b) is extracted from [37] directly, which is constructed based on some experimental and theoretical works [38–46]. The agreement demonstrates the accuracy and reliability of our calculations. In Fig. 4(a), we also show the comparison of intrinsic conductivities of TLG and MLG along the x direction calculated by using iteration method for Fermi energy in the range -0.2–0.2 eV. This energy range is still in the linear band region and corresponds to the carrier concentration -0.2–0.2×10^{13} cm^{-2} for TLG [see Fig. 4(c)]. This carrier concentration can be realized readily experimentally for two-dimensional materials [47,48]. In Fig. 4(a), the conductivities of the MLG around the Dirac point are not shown, because the Boltzmann equation we adopt is a semiclassical theory, which fails to predict the correct conductivity of MLG around the Dirac point because there are strong quantum coherence effects between the electronic waves with long wavelength, and the coherence effects are not covered by the Boltzmann equation. Hereinafter, only the conductivity along the x direction is discussed due to its isotropy as shown in Fig. 4(d). With the Dirac points of MLG and TLG used as the energy references and at the same Fermi energy (E_f), the linear dispersion bands in TLG and MLG can host the same number of carriers, and they have the same Fermi surface. Therefore, in the sight of band structure, the linear dispersion bands in TLG and MLG should contribute the same conductivity, and TLG should have larger total intrinsic conductivity due to the additional contribution from its parabolic bands. Such a prediction can be verified by calculating and comparing their intrinsic conductivities [see Fig. 5(a)] under the constant relaxation time approximation for all electronic states, i.e., $\tau_{nk} = \tau$, because the results given in Fig. 5(a) reflect the sole contribution of the band structure on the conductivity. However, after considering the e-ph scattering, our numerical results [see Fig. 4(a)] show that the additional parabolic bands spanning the Fermi level do not result in a larger intrinsic conductivity in TLG, but 20% smaller at $E_f > 0.1$ eV and 50% smaller at hole doping, in comparison with MLG. These results mean that the e-ph scattering is much stronger in TLG than MLG, which results in a smaller intrinsic conductivity.

C. The reason for the conductivity reduction of TLG

To understand the origin of the decrease in conductivity, it is necessary to perform a detailed study on the e-ph scattering in TLG. In Fig. 5(b), we show the numerical results of the e-ph scattering rates [defined in Eq. (7)] for the electronic states in the energy range 0.05–0.2 eV. The corresponding results of MLG are also given for comparison. It can be found that the scattering rates of TLG are obviously larger than those in MLG for the whole energy range, which can well account for the relatively small intrinsic conductivity of TLG compared with MLG. Moreover, if we calculate the scattering rates for the states in the linear or parabolic dispersion band by restricting the scattering final state in the same band, namely, we only count in the contribution of intraband scattering. The results shown in Fig. 5(b) indicate that the intraband scattering rates in TLG are even smaller than the ones in MLG. Consequently, the linear dispersion band in TLG can contribute a higher conductivity than that in MLG if only intraband scattering is considered, which is verified by the numerical results shown in Fig. 4(a). The reason that the intralinear-band-scattering rates in TLG are smaller than those in MLG lies in the difference of the low-frequency phonon dispersions as shown

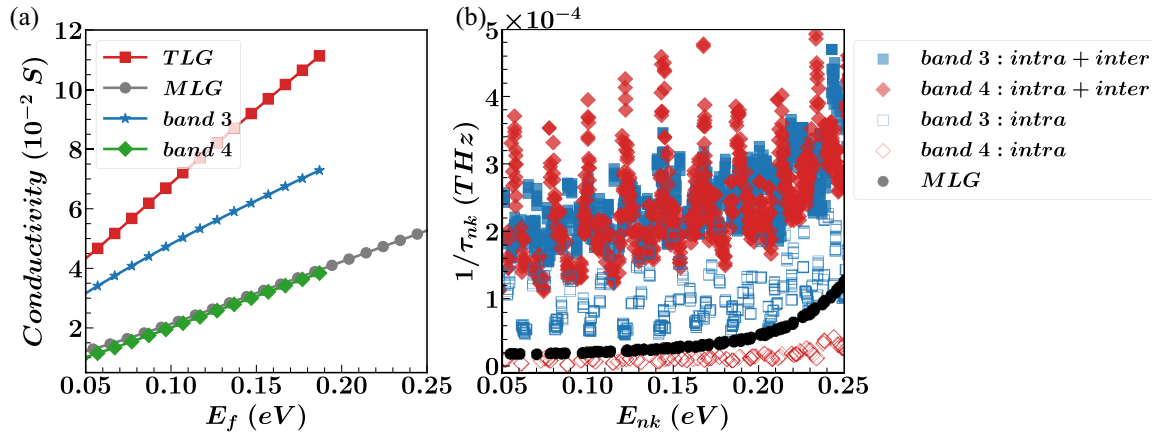

FIG. 5. (a) Conductivities of TLG and MLG calculated by using the constant relaxation time approximation with $\tau = 0.05$ fs. Blue and green lines are the contributions of bands 3 and 4 in TLG, respectively. (b) Electron-phonon scattering rates in TLG for electrons in the energy range of 0.05–0.25 eV. Full (empty) squares and diamonds correspond to the electrons in bands 3 and 4 with the intraplus interband (only intraband) scatterings under consideration. The electron-phonon scattering rates in MLG are given in black dots for comparison. Bands 3 and 4 are the parabolic and linear bands as shown in Fig. 2. In (a) and (b), the Dirac points of MLG and TLG are used as the energy references.

in Fig. 3(b). Due to the interlayer coupling, the degenerate ZA modes of three isolated layers (one ZA mode for one layer) evolve into one acoustic mode (ZA) and two optical modes (ZO) in TLG, and the frequencies of the two optical modes are pushed upwards around Γ point. This evolution also occurs in the degenerate LA and TA modes. Just due to such a rising of frequency, these optical phonon modes are less excited for scattering carriers in the TLG, in contrast to their predecessor, i.e., the acoustic phonon modes in the MLG. As a result, the scattering rates of the electron states in the linear band of TLG are notably smaller than the case in MLG. Hence the conductivity of TLG contributed from the linear bands is larger than that of MLG. All of our numerical results and analysis indicate that the interband scatterings between the linear and parabolic dispersion bands play the key role on limiting the intrinsic conductivity of TLG.

From the lattice structure shown in Fig. 1, one can easily find that the TLG has the mirror symmetry with respect to the middle layer, and we label the mirror operation as $\hat{M}_z$. Therefore both the electronic and phonon states are also the eigenstates of $\hat{M}_z$, and the eigenvalues of 1 and -1 for $\hat{M}_z$ correspond to the even- and odd-parity states. The electronic states from the linear and parabolic bands as shown in Fig. 2 are the even- and odd-parity states, respectively. All of the even- and odd-parity phonon states at low frequency are plotted in green and blue as shown in Fig. 3(b). When the electron-phonon coupling is under consideration, whether one scattering process occurs or not is governed by the selection rule (see Table I) due to the existence of the mirror symmetry, where one scattering process means that one electron is scattered from one state to another by one phonon which is described by the scattering matrix element $g^{m,\boldsymbol{k}+\boldsymbol{q}}_{\boldsymbol{nk},\boldsymbol{q}\nu}$ [see Eq. (5)]. For the interband scatterings, the initial and final electronic states have the opposite parties, so only the odd functions $\partial_{\boldsymbol{q}\nu}V$, which correspond to the even-parity phonon states, contribute the interband scattering conductivity according to the selection rule. Our results demonstrate that the ZA, lowest LO and TO, and second lowest ZO phonons have the even-parity states and contribute the interband scattering.

To demonstrate the importance of symmetry for restricting the intra- and interband scatterings, there is a need to compare the e-ph interaction strength among the low-frequency phonon modes, just as done in the previous literatures [33,49,50]. In so doing, we define the quantity

$$\gamma^{\nu}_{nm}(\boldsymbol{q}) = \frac{N_{\boldsymbol{q}\nu}}{N_{\boldsymbol{k}}} \sum_{\boldsymbol{k}} \left| g^{m\boldsymbol{k}+\boldsymbol{q}}_{n\boldsymbol{k},\boldsymbol{q}\nu} \right|^2 \delta(E_{n\boldsymbol{k}} - E_f)\delta(E_{m\boldsymbol{k}+\boldsymbol{q}} - E_f), \quad (9)$$

which is the phonon linewidth [51] weighed by the phonon number. Please note that the restriction of the initial and final electronic states on the Fermi energy does not mean that the phonon energy vanishes because the e-ph interaction matrix element $g^{m\boldsymbol{k}+\boldsymbol{q}}_{n\boldsymbol{k},\boldsymbol{q}\nu}$ does not respect energy conservation. The value of $\gamma^{\nu}_{nm}(\boldsymbol{q})$ is just an average of the e-ph interaction matrix elements on the Fermi surface. Hence it is not equivalent to the e-ph scattering rate which obeys the energy conservation. But we can use such a quantity to account for the numerical results of the e-ph scattering rate, especially the symmetry prohibition of some scattering processes. As an example, the values of $\gamma^{\nu}_{nm}(\boldsymbol{q})$ for the intra- and interband e-ph couplings at $E_f = 0.2$ eV and under the temperature of 300 K are calculated numerically and plotted in Fig. 3(c), where only the low-frequency phonons with $|\boldsymbol{q}| < 0.1\pi/a$ are considered, because $0.1\pi/a$ is very close to the average spacing between the two pieces of the Fermi surfaces and only low-frequency phonons are excited effectively at room temperature. Our

TABLE I. Selection rule for scattering processes with nonzero e-ph coupling matrix element $g^{m\boldsymbol{k}+\boldsymbol{q}}_{n\boldsymbol{k},\boldsymbol{q}\nu}$. $\varphi_{n\boldsymbol{k}}$ and $\varphi_{m\boldsymbol{k}+\boldsymbol{q}}$ are the initial and final electronic states, and $\phi_{\boldsymbol{q}\nu}$ is the phonon state. $\partial_{\boldsymbol{q}\nu}V$ and phonon state $\phi_{\boldsymbol{q}\nu}$ always have the opposite parities.

Scattering	$\varphi_{n\boldsymbol{k}}$	$\varphi_{m\boldsymbol{k}+\boldsymbol{q}}$	$\partial_{\boldsymbol{q}\nu}V$	$\phi_{\boldsymbol{q}\nu}$
intraband	odd	odd	even	odd
intraband	even	even	even	odd
interband	odd	even	odd	even
interband	even	odd	odd	even

results indicate that the e-ph coupling respects the symmetry restriction. That is the even- and odd-parity phonons [the green and blue lines in Fig. 3(b)] take part in only the inter- and intraband scatterings, respectively. Among these phonon modes, the *ZA* phonon mode in the long-wavelength region contributes the interband scattering more than 50%, so it is the most important phonon mode for limiting the intrinsic conductivity of TLG. This result can be attributed to the fact that, compared with other phonons, the number of *ZA* phonons is largest because it has the smallest dispersion and lowest frequency [see Fig. 3(b)]. But the *ZA* phonon mode is absent for the intraband scattering due to the prohibition of the mirror symmetry in spite of the existence of a large number of *ZA* phonons. As we have discussed above, the intraband scattering can not well explain the small intrinsic conductivity of TLG compared with MLG. Therefore we can say that the *ZA* phonons in the long-wavelength region have the key effect for limiting the intrinsic conductivity of TLG.

D. Discussion

As aforementioned in the introduction section, there are naturally two kinds of trilayer graphenes. The ABC-stacked TLG is a semiconductor with the Fermi level just at the band touching point where the carrier concentration vanishes and the Fermi surface is small, just like the case of MLG. Thus, the semiclassical BTE seems invalid for well describing the e-ph scattering limited conductivity because of the strong quantum coherence effects. As for the case of carrier doping, our numerical results within BTE (not shown in the present work) indicate that the ABC-stacked TLG has a room temperature conductivity limited by e-ph scattering comparable to its counterpart of the ABA-stacked TLG as discussed above when the Fermi level is away from the band touching point by at least 0.1 eV. According to our findings, the mirror symmetry M_z of MLG prohibits the ZA phonon being involved in the intraband scattering, but the ZA mode has the crucial effect on the intrinsic conductivity of ABA-stacked TLG via interband scattering. Such an argument can be generalized to thicker graphene multilayers with ABA stacking and odd number layer since the same mirror symmetry remains. As for ABC-stacked TLG, mirror symmetry M_z is broken but 3D spatial inversion symmetry appears, and the effect of the symmetry on the conductivity of ABC-stacked TLG is under our current study.

Just like the case of MLG, the linear dispersion bands in ABA-stacked TLG form a pair of circular Fermi surfaces centered at K and K' points (two inequivalent k points at the hexagonal BZ corners). According to our numerical results, the warping of the Fermi surface from a circle can be safely ignored within 0.4 eV relative to the Dirac point. Thus, there must appear a strong nesting effect between the two circular Fermi surfaces connected by the so-called nesting wave vector of $q_0 = |\boldsymbol{K}|$. Usually, the Fermi surface nesting effect implies strong e-ph scattering when the phonon wave vector agrees with the nesting wave vector. Hence such a nesting effect is expected to affect the intrinsic conductivity sizeably. However, our calculations indicate that the nesting effect on the intrinsic conductivity of ABA-stacked TLG at room temperature is so trivial that it can be safely ignored. The underlying reason is simple. As shown in the phonon spectrum in Fig. 3(a), even for the lowest phonon frequency with the nesting wave vector, for example at K point, the corresponding thermal excitation temperature is about 800 K, much larger than 300 K. It means that at room temperature such a phonon mode has not been excited effectively. Consequently, it can not bring about any nontrivial nesting effect.

In this work, we are mainly concerned with the ZA phonons which play the important role to limit the intrinsic conductivity of ABA-stacked TLG due to the nontrivial interband e-ph scattering. However, it does not mean that other phonon modes are always less important than ZA phonons to influence other electronic properties of TLG dominated by e-ph interaction such as the superconductivity and optical adsorption. Therefore, before ending our work, it is significant to compare the e-ph interactions associated with various phonon modes in the ABA-stacked TLG. In so doing, we choose to show phonon mode resolved Eliashberg spectral function which is much involved in all physical properties dominated by the e-ph coupling. For example, in the Migdal-Eliashberg theory, a more systematic superconductivity theory than the simple Mcmillian-Allen-Dynes formula, the Eliashberg spectral function is the central physical quantity. This spectral function is defined by

$$\alpha^2F(\omega) = \frac{1}{N(E_f)}\sum_{\boldsymbol{q}\nu}\delta(\omega-\omega_{\boldsymbol{q}\nu})\gamma_{\boldsymbol{q}\nu}, \tag{10}$$

which consists of the contributions of all phonon modes, namely $\alpha^2F(\omega) = \sum_\nu \alpha^2F^\nu(\omega)$, and $\alpha^2F^\nu(\omega)$ reads

$$\alpha^2F^\nu(\omega) = \frac{1}{N(E_f)}\sum_{\boldsymbol{q}}\delta(\omega-\omega_{\boldsymbol{q}\nu})\gamma_{\boldsymbol{q}\nu}, \tag{11}$$

where $N(E_f)$ is the electronic density of states at Fermi energy, and $\gamma_{\boldsymbol{q}\nu}$ is the linewidth for phonon with mode ν and wave vector $\boldsymbol{q}$, which is defined by

$$\gamma_{\boldsymbol{q}\nu} = \sum_{nm}\frac{\gamma^\nu_{nm}(\boldsymbol{q})}{N_{\boldsymbol{q}\nu}}. \tag{12}$$

Our calculated spectral function of ABA-stacked TLG and the contributions of eighteen phonon modes when Fermi energy is at 0.2 eV above the charge neutrality point are shown in Fig. 6. Our results indicate that the spectral function peaks exist only in three frequency regions, such as the low-frequency region less than 200 cm^{-1} contributed by the phonon modes 1–9 evolved from only the acoustic phonon modes of MLG, the middle frequency region around 900 cm^{-1} contributed by the phonon modes 10–12 evolved from the optical ZO modes of MLG, and high-frequency region more than 1500 cm^{-1} contributed by the phonon modes 13–18 evolved from the optical TO and LO modes of MLG. Among the three frequency regions, the peaks in the low-frequency region dominate the superconducting properties. Compared with the ZA mode (mode 1 in Fig. 6), the contributions of modes 6 and 7 (the second TO and LO modes originated from the acoustic TA and LA modes of MLG) to the spectral function and the superconducting properties should be much stronger, although they influence the intrinsic conductivity of TLG weaker than the ZA mode.

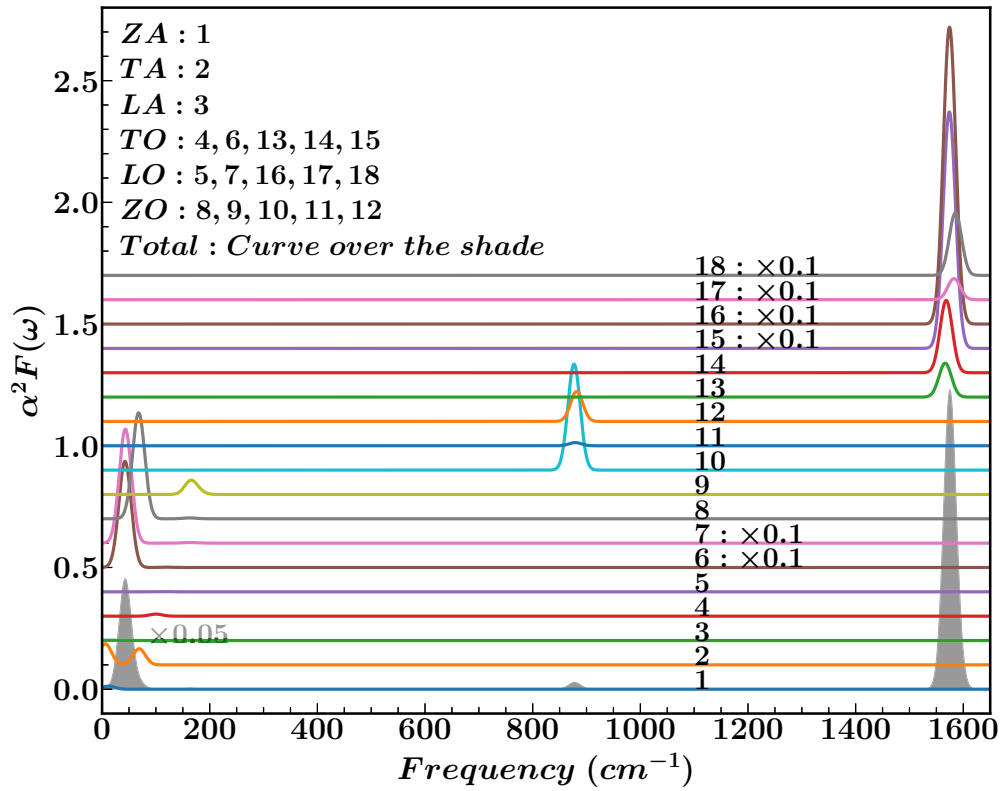

FIG. 6. The spectral function $\alpha^2F(\omega)$ of ABA-stacked TLG with the contributions of all eighteen phonon modes $\alpha^2F^{\nu}(\omega)$ for Fermi energy at 0.2 eV above the charge neutrality point. The spectral functions of 18 phonon modes labeled from 1 to 18 are shifted upwards by different values for comparison. The total spectral function plotted in shade is multiplied by 0.05, and the spectral function values of the phonon modes 6, 7, 15, 16, 17, and 18 are multiplied by 0.1.

Recently, the e-ph couplings in ABC-stacked TLG also attract much of attention because of the experimental observation of the exotic superconductivity [17], which was explained as the acoustic-phonon-mediated conventional superconductivity based on a simple model of the e-ph interaction in theory [16]. However, the quantitative accuracy of this simple model is questionable, so it is a necessary and interesting topic to study systematically the phonon-mediated superconducting behavior of ABC-stacked TLG by means of the full first-principles calculations based on the Migdal-Eliashberg formalism.

IV. MAIN CONCLUSION

In summary, within the theoretical framework of the BTE, we study systematically the room-temperature conductivity of ABA-stacked TLG limited by e-ph scattering. All the required quantities such as the electronic band structure, the phonon frequency and e-ph interaction matrix elements are obtained by performing the first-principles calculations. Then, by employing the Wannier interpolation technique, we can obtain the reliable numerical results of the conductivity of TLG with high precision. Firstly, we find that the ABA-stacked TLG is a semimetal since there are a linear dispersion band, together with a parabolic dispersion band spanning the Fermi level, reminiscent of a combination of the band structures of a mono- and bilayer graphene. Then, our calculations indicate that the conductivity of such a TLG is always smaller than that in a monolayer graphene roughly by 20% when the carrier concentration varies in a moderate doping range though the TLG has more than one band spanning the Fermi level to contribute the conductivity. To explain such a disagreement between the band structure and the calculated result of the conductivity of TLG, we find that the out-of-plane vibration, i.e., the *ZA* phonon modes in the long-wavelength region, plays the critical role on limiting the conductivity of TLG, which brings about the strong e-ph scattering between the linear and parabolic bands with opposite parities, which is allowed by the mirror symmetry in TLG. In contrast, the *ZA* phonon mode is completely decoupled from the e-ph scattering in the MLG in which there is only one linear dispersion band around the Fermi level. The mirror symmetry prevents the *ZA* phonon from the intraband scattering. In short, in ABA-stacked TLG the nontrivial interband scattering arising from the *ZA* phonon has the predominate suppression on the room temperature conductivity. Consequently, the TLG has a relatively weak electronic transport ability at room temperature. However, in view of the ultrahigh conductivity of MLG, our numerical result indicates that the TLG is still a good conductor under a moderate carrier doping.

ACKNOWLEDGMENTS

This work was financially supported by the National Natural Science Foundation of China (Grants No. 12174145 and No. 11774123) and the National Science Foundation

for Young Scientists of China (Grants No. 11404132, No. 11504125, and No. 11504319). We thank the High Performance Computing Center of Jilin University for their calculation resource.

[1] W. Bao, L. Jing, J. Velasco, Y. Lee, G. Liu, D. Tran, B. Standley, M. Aykol, S. B. Cronin, D. Smirnov, M. Koshino, E. McCann, M. Bockrath, and C. N. Lau, Nat. Phys. **7**, 948 (2011).
[2] C. H. Lui, Z. Li, K. F. Mak, E. Cappelluti, and T. F. Heinz, Nat. Phys. **7**, 944 (2011).
[3] A. F. Morpurgo, Nat. Phys. **11**, 625 (2015).
[4] T. Taychatanapat, K. Watanabe, T. Taniguchi, and P. Jarillo-Herrero, Nat. Phys. **7**, 621 (2011).
[5] M. F. Craciun, S. Russo, M. Yamamoto, J. B. Oostinga, A. F. Morpurgo, and S. Tarucha, Nat. Nanotechnol. **4**, 383 (2009).
[6] F. Zhang, B. Sahu, H. Min, and A. H. MacDonald, Phys. Rev. B **82**, 035409 (2010).
[7] A. A. Avetisyan, B. Partoens, and F. M. Peeters, Phys. Rev. B **81**, 115432 (2010).
[8] W. Jaskólski and G. Sarbicki, Phys. Rev. B **102**, 035424 (2020).
[9] S. Che, P. Stepanov, S. Ge, M. Zhu, D. Wang, Y. Lee, K. Myhro, Y. Shi, R. Chen, Z. Pi, C. Pan, B. Cheng, T. Taniguchi, K. Watanabe, Y. Barlas, R. K. Lake, M. Bockrath, J. Hwang, and C. N. Lau, Phys. Rev. Lett. **125**, 246401 (2020).
[10] H. Wu, X. Yu, M. Zhu, Z. Zhu, J. Zhang, S. Zhang, S. Qin, G. Wang, G. Peng, J. Dai, and K. S. Novoselov, J. Phys. Chem. Lett. **12**, 7328 (2021).
[11] L.-J. Yin, L.-Z. Yang, L. Zhang, Q. Wu, X. Fu, L.-H. Tong, G. Yang, Y. Tian, L. Zhang, and Z. Qin, Phys. Rev. B **102**, 241403(R) (2020).
[12] Z. Ge, S. Slizovskiy, F. Joucken, E. A. Quezada, T. Taniguchi, K. Watanabe, V. I. Fal'ko, and J. Velasco, Phys. Rev. Lett. **127**, 136402 (2021).
[13] H. Zhou, T. Xie, A. Ghazaryan, T. Holder, J. R. Ehrets, E. M. Spanton, T. Taniguchi, K. Watanabe, E. Berg, M. Serbyn, and A. F. Young, Nature (London) **598**, 429 (2021).
[14] H. Dai, J. Hou, X. Zhang, Y. Liang, and T. Ma, Phys. Rev. B **104**, 035104 (2021).
[15] A. Ghazaryan, T. Holder, M. Serbyn, and E. Berg, Phys. Rev. Lett. **127**, 247001 (2021).
[16] Y.-Z. Chou, F. Wu, J. D. Sau, and S. Das Sarma, Phys. Rev. Lett. **127**, 187001 (2021).
[17] H. Zhou, T. Xie, T. Taniguchi, K. Watanabe, and A. F. Young, Nature (London) **598**, 434 (2021).
[18] S. Chatterjee, T. Wang, E. Berg, and M. P. Zaletel, Inter-valley coherent order and isospin fluctuation mediated superconductivity in rhombohedral trilayer graphene, arXiv:2109.00002 [cond-mat.supr-con].
[19] M. Huang, P. V. Bakharev, Z.-J. Wang, M. Biswal, Z. Yang, S. Jin, B. Wang, H. J. Park, Y. Li, D. Qu, Y. Kwon, X. Chen, S. H. Lee, M.-G. Willinger, W. J. Yoo, Z. Lee, and R. S. Ruoff, Nat. Nanotechnol. **15**, 289 (2020).
[20] Z. Gao, S. Wang, J. Berry, Q. Zhang, J. Gebhardt, W. M. Parkin, J. Avila, H. Yi, C. Chen, S. Hurtado-Parra, M. Drndić, A. M. Rappe, D. J. Srolovitz, J. M. Kikkawa, Z. Luo, M. C. Asensio, F. Wang, and A. T. C. Johnson, Nat. Commun. **11**, 546 (2020).
[21] E. A. Henriksen, D. Nandi, and J. P. Eisenstein, Phys. Rev. X **2**, 011004 (2012).
[22] H. Liu, H. Jiang, and X. C. Xie, AIP Adv. **2**, 041405 (2012).
[23] W. Kohn and L. J. Sham, Phys. Rev. **140**, A1133 (1965).
[24] S. Baroni, S. de Gironcoli, A. Dal Corso, and P. Giannozzi, Rev. Mod. Phys. **73**, 515 (2001).
[25] T.-H. Liu, J. Zhou, B. Liao, D. J. Singh, and G. Chen, Phys. Rev. B **95**, 075206 (2017).
[26] T. Sohier, D. Campi, N. Marzari, and M. Gibertini, Phys. Rev. Mater. **2**, 114010 (2018).
[27] W. Li, J. Carrete, N. A. Katcho, and N. Mingo, Comput. Phys. Commun. **185**, 1747 (2014).
[28] W. Li, Phys. Rev. B **92**, 075405 (2015).
[29] P. Giannozzi, O. Andreussi, T. Brumme, O. Bunau, M. Buongiorno Nardelli, M. Calandra, R. Car, C. Cavazzoni, D. Ceresoli, M. Cococcioni, N. Colonna, I. Carnimeo, A. Dal Corso, S. de Gironcoli, P. Delugas, J. DiStasio, R. A., A. Ferretti, A. Floris, G. Fratesi, G. Fugallo *et al.*, J. Phys.: Condens. Matter **29**, 465901 (2017).
[30] N. Troullier and J. L. Martins, Phys. Rev. B **43**, 1993 (1991).
[31] J. P. Perdew, K. Burke, and M. Ernzerhof, Phys. Rev. Lett. **77**, 3865 (1996).
[32] F. Giustino, M. L. Cohen, and S. G. Louie, Phys. Rev. B **76**, 165108 (2007).
[33] S. Poncé, E. Margine, C. Verdi, and F. Giustino, Comput. Phys. Commun. **209**, 116 (2016).
[34] M. G. Menezes and R. B. Capaz, J. Phys.: Condens. Matter **27**, 335302 (2015).
[35] C. H. Lui, Z. Ye, C. Keiser, E. B. Barros, and R. He, Appl. Phys. Lett. **106**, 041904 (2015).
[36] L. Wang, I. Meric, P. Y. Huang, Q. Gao, Y. Gao, H. Tran, T. Taniguchi, K. Watanabe, L. M. Campos, D. A. Muller, J. Guo, P. Kim, J. Hone, K. L. Shepard, and C. R. Dean, Science **342**, 614 (2013).
[37] L. Banszerus, T. Sohier, A. Epping, F. Winkler, F. Libisch, F. Haupt, K. Watanabe, T. Taniguchi, K. Müller-Caspary, N. Marzari, F. Mauri, B. Beschoten, and C. Stampfer, Extraordinary high room-temperature carrier mobility in graphene-wse$_2$ heterostructures, arXiv:1909.09523 [cond-mat.mes-hall].
[38] C. R. Dean, A. F. Young, I. Meric, C. Lee, L. Wang, S. Sorgenfrei, K. Watanabe, T. Taniguchi, P. Kim, K. L. Shepard, and J. Hone, Nat. Nanotechnol. **5**, 722 (2010).
[39] J.-H. Chen, C. Jang, S. Xiao, M. Ishigami, and M. S. Fuhrer, Nat. Nanotechnol. **3**, 206 (2008).
[40] K. Zou, X. Hong, D. Keefer, and J. Zhu, Phys. Rev. Lett. **105**, 126601 (2010).
[41] D. K. Efetov and P. Kim, Phys. Rev. Lett. **105**, 256805 (2010).
[42] E. H. Hwang and S. Das Sarma, Phys. Rev. B **77**, 115449 (2008).
[43] T. Sohier, M. Calandra, C.-H. Park, N. Bonini, N. Marzari, and F. Mauri, Phys. Rev. B **90**, 125414 (2014).
[44] L. Pietronero, S. Strässler, H. R. Zeller, and M. J. Rice, Phys. Rev. B **22**, 904 (1980).

[45] V. Perebeinos and P. Avouris, Phys. Rev. B **81**, 195442 (2010).
[46] C.-H. Park, N. Bonini, T. Sohier, G. Samsonidze, B. Kozinsky, M. Calandra, F. Mauri, and N. Marzari, Nano Lett. **14**, 1113 (2014).
[47] E. Piatti, D. De Fazio, D. Daghero, S. R. Tamalampudi, D. Yoon, A. C. Ferrari, and R. S. Gonnelli, Nano Lett. **18**, 4821 (2018).
[48] J. T. Ye, Y. J. Zhang, R. Akashi, M. S. Bahramy, R. Arita, and Y. Iwasa, Science **338**, 1193 (2012).
[49] A. N. Rudenko and S. Yuan, Phys. Rev. B **101**, 115127 (2020).
[50] Q. Tang, L. A. Svyatkin, and I. P. Chernov, Phys. Rev. B **99**, 205152 (2019).
[51] J. Noffsinger, F. Giustino, B. D. Malone, C.-H. Park, S. G. Louie, and M. L. Cohen, Comput. Phys. Commun. **181**, 2140 (2010).